# Fault flexure and lithosphere rheology set from climate cycles record in the Corinth Rift

Gino de Gelder[1*], David Fernández-Blanco[1], Daniel Melnick[2,3], Guillaume Duclaux[4,5], Rebecca E. Bell[6], Julius Jara-Muñoz[2], Rolando Armijo[1] and Robin Lacassin[1]

1) Institut de Physique du Globe de Paris, Sorbonne Paris Cité, Université Paris Diderot, UMR 7154 CNRS, 1 Rue Jussieu, F-75005, Paris, France

2) Institut für Erd- und Umweltwissenschaften, Universität Potsdam, Karl-Liebknecht-Strasse 24, 14476 Potsdam, Germany

3) Facultad de Ciencias, Universidad Austral de Chile, Casilla 567, Valdivia, Chile

4) Department of Earth Science, University of Bergen, Bergen N-5020, Norway

5) Université Côte d'Azur, CNRS, OCA, IRD, Géoazur, 06560 Valbonne, France

6) Basins Research Group (BRG), Department of Earth Science & Engineering, Imperial College, Prince Consort Road, London SW7 2BP, UK

*Corresponding author: gelder@ipgp.fr

**Abstract**

Geomorphic strain markers accumulating the effects of many earthquake cycles help to constrain the mechanical behaviour of continental rift systems as well as related seismic hazard. In the Corinth Rift (Greece), the remarkably rich record of onshore and offshore markers of Pleistocene 100ky climate cycles is unique worldwide and makes it a key site to constrain rift mechanics on a large range of timescales. We use high-resolution topography to analyse the 3D geometry of well-exposed and dated Late Pleistocene marine terraces uplifted by flexure on the southern rift shoulder. This dataset is completed offshore with seismic data imaging the

flexure across the present-day rift basin. We find 4.5-6.7mm·yr$^{-1}$ of average slip rate on the master fault over the past ~610ka and an uplift/subsidence ratio of 1:1.2-2.4. To reproduce the uplift and subsidence flexure patterns, we use a 3-layered finite element model at lithospheric scale. Results imply a 40-60° planar normal fault through the elastic upper crust, and a lower crust more viscous than the upper mantle beneath the Corinth Rift. We suggest that such a rheology may typify rapid localised extension of continental lithosphere.

**Main text**

Extension in continental rifts is characterised by normal faulting in the seismogenic upper crust, and a combination of brittle and/or ductile deformation in the underlying lower crust and upper mantle[1]. Our primary understanding of lithospheric structure and rheological layering under such rifts is based on observations of the earthquake cycle at short timescales ($10^0$-$10^3$ yr)[2–5], or evolved mature rift systems formed over geological timescales ($10^6$-$10^8$ yr)[6–9]. However, observations of deformation in modern continental rifts - as documented by geology and geomorphology thus accumulating the effects of many earthquake cycles - allows for incorporating crustal deformation at spatial scales of tens of km integrated on timescales of $10^4$-$10^6$ yr. Here we aim at characterizing lithospheric rheology and extension mechanisms of the young and very fast-evolving Corinth Rift in Greece (Fig. 1), an asymmetric rift born in the Pleistocene[10,11]. Along the rift southern shoulder, a 130-km-long north-dipping fault system controls downward flexure associated with more than 3-km of hanging-wall subsidence[12], counterbalanced by upward flexure associated with about 2-km of footwall uplift at rates of ~1.3 mm·yr$^{-1}$ [10]. Footwall flexure has clearly deformed a set of Pleistocene terraces correlated with 100-ky climate cycles and dramatically modified the modern evolution of river drainages.

The global ~100 ky glacial-interglacial cycles correlate well with the most important variations of global temperatures and sea-level over the past 1200-800 ky[13,14]. In the Corinth Rift, sea-level variations have left their imprint on both sides of the main north-dipping fault system. In the

onshore domain to the south, the superposition of glacio-eustatic sea-level variations on rapid tectonic uplift and flexure resulted in increasingly deforming sequences of wave-cut marine terraces (Fig. 1). In the offshore hanging-wall domain, two bathymetric sills[15] controlled sedimentation in the Gulf as a function of the same sea-level variations, switching rhythmically from lacustrine environment during sea-level lowstands to marine during sea-level highstands[16,17]. Taking advantage of this exceptional geological setting and record, we focus our high-resolution analysis on the uplifted marine terraces between the towns of Corinth and Xylokastro (Fig. 1) where previous studies revealed a systematic elevation decrease with distance from the main north-dipping fault system[10]. We use a high-resolution onshore topographic dataset to resolve accurately the terrace uplift and flexure pattern. We then complete the analysis with depth-converted offshore seismic data[18] to provide a unique integrated view of the flexure due to continental rifting. Based on these data, numerical modelling allows us to resolve the primary rheological parameters controlling lithospheric deformation in such young rifts. This study provides new constraints on the dynamics of the Corinth rift system, both critical for understanding active deformation and its controlling mechanisms at thousand- to million-years time-scales.

**Uplifted Marine terraces**

Earlier studies described the outstanding flight of marine terraces in the Corinth Rift[19–20], which are similar to the present-day shoreline of the Gulf but are now uplifted to elevations of up to 400 m (Fig. 1 and Supplementary Fig. 1). It was shown that those palaeo-shorelines could be used to describe the progressive uplift and flexure of originally horizontal lines that were at sea-level and synchronous with main interglacial peaks[10]. So their gradually deformed geometry may be used as a “palaeo-geodetic” data set, which when integrated with numerical modelling experiments may help derive mechanical characteristics of the Corinth Rift’s evolution.

The Corinth terraces are generally composed of abrasion surfaces in soft Plio-Quaternary marls, sandstones and conglomerates, and are unconformably overlain by 2-6 m of erosion-resistant caprock consisting of well-cemented coastal deposits (Supplementary Fig. 2). In the area between Corinth and Xylokastro, we calculated a 2m-resolution Digital Surface Model (DSM) from Pleiades satellite imagery. This DSM allows us to observe the morphology of terraces with far greater detail than a typical open-source Digital Elevation Model, to quantify the 3D terrace geometry (Fig. 2; Supplementary Fig. 3).

The terraces are typically bounded inland by a palaeocliff. The intersection between terrace and palaeocliff, or shoreline angle (Supplementary Fig. 2), is considered the most appropriate datum of past sea-level position during the highstand they were formed[21,22]. We focus on the shoreline angles of terraces formed during major interglacial highstands (Fig. 3b), that are the best preserved here[10] and globally[23], and their corresponding glacio-eustatic sea-level less uncertain than lower interstadial highstands[24]. We adopt the proposed terrace names by Armijo et al.[10]. Our high-resolution analysis detects more terrace sub-levels than previous studies, hence we add Roman numerals to distinguish between those sub-levels. They serve as guidelines for a precise spatial correlation across the whole flight of terraces, which increases the accuracy to determine the flexured geometry of the main interglacial highstands and particularly to unravel the geometry of the more eroded levels older than the Old Corinth terrace (~240 ka). This improved approach does not significantly change however the interpretation of Armijo et al.[10] for the New Corinth (here New Corinth (II)) and Old Corinth (here Old Corinth (II)) terraces. Consequently, the shoreline angles determined for those two terraces correlate unambiguously with the two first major interglacial highstands preceding the present-day one, specifically with Marine Isotope Stage (MIS) 5e (~124 ka) and MIS 7e (~240 ka) respectively (Fig. 3b), in agreement with U/Th coral datings[25–27] and IcPD dating of *Pecten*[28]. Uplift rates derived for the shorelines of those two well-known major interglacial highstands are very similar (~0.3-1.3 $mm \cdot yr^{-1}$, Supplementary Fig. 4), suggesting time-constant uplift rates for the Corinth terraces

over the past ~240 kyr. For older major interglacial highstands, our refined geometry and updated knowledge of glacio-eustatic sea-level variation leads us to propose correlation of the Temple (II) and Laliotis terraces to interglacial highstands MIS 9e (~326 ka) and MIS 11c (~409 ka) respectively, in better agreement than Armijo et al.[10] with assumed time-constant uplift rates (Supplementary Fig. 4). With the same assumption, terraces older than the designated Unnamed and Nicoletto would correspond to MIS 13e (~505 ka) and MIS 15c (~605 ka) respectively (Fig. 3b), but these old levels are significantly degraded and laterally discontinuous. All of the other terrace levels should correspond to interstadial sea-level highstands lower than today's sea level. Those interstadial levels are more numerous and better preserved close to the Xylokastro Fault (Fig. 2), where the footwall uplift rate is highest (~1.3 $mm \cdot yr^{-1}$).

The first order signal of the best-preserved terraces indicates a broad footwall flexure of at least ~20 km in relation to the Xylokastro on- and offshore faults and Lykoporia Fault (Fig. 1 and 2). To estimate the long-term maximum uplift rate closest to this fault system we extrapolated the combined uplift rates of the New Corinth (II), Old Corinth (II), Temple (II) and Laliotis shoreline angles, obtaining an uplift rate of 1.63±0.12 $mm \cdot yr^{-1}$, or 1.72±0.08 $mm \cdot yr^{-1}$ if we exclude the slightly lower uplift rates of the New Corinth (II) terrace (Supplementary Fig. 4).

**Rift-scale cross-section**

The Rion sill in the western Gulf, presently at 62 m depth[29], and the Corinth Isthmus in the eastern Gulf (Fig. 1), presently onshore, limited the water exchange during sea-level lowstands between the Gulf and the open sea over the past 600-700 ka[16], so they may be responsible for the alternating marine/lacustrine sedimentation found now both on- and offshore[17,18,30]. Long piston cores through the last lacustrine-marine transition ~13 ka[31] have been calibrated with seismic profiles. On the basis of the seismic character of this transition, several studies have interpreted the base horizon of deeper high amplitude packages as older lacustrine-marine transitions and correlated these to glacio-eustatic sea-level curves[12,18,32,33] down to the basin-

wide unconformity U (Fig. 3). We used the most recent interpretation of seismic stratigraphy, faults and velocity model[33] to depth-convert seismic line L35 of Taylor et al.[18], and combined it with the onshore topography across the Klimenti Gilbert-type delta and the shoreline angles of major interglacial terrace levels (Fig. 3). If the proposed offshore ages are correct, the timing of on- and offshore markers is remarkably similar. Small systematic differences of ~5-15 ka then correspond to delays between lacustrine to marine transitions and the maximum sea-level stands reached at the climax of interglacials (Fig. 3).

The cross-section suggests that ~60-70% of the deformation associated with the Xylokastro and Lykoporia faults has occurred over the past ~610 ka, assuming that the highest Klimenti delta foresets onshore and deepest sediments offshore are age-equivalent to the onset of faulting. Before ~610 ka, detailed interpretation is hindered by the lack of well-developed marine terraces onshore and lack of mappable seismic horizons offshore. The most elevated marine deposits in this area are found near Souli (Fig. 3), and have been tentatively dated as <450 ka[20] using nannoplankton, an age that we disregard since it would require an unreasonably high deceleration of uplift rate with respect to the more reliably dated New and Old Corinth terraces (from ~2.1 to ~0.7 $mm \cdot yr^{-1}$ at 10 km from the fault). We do note the similarity in geometrical position between these highest marine deposits onshore and oldest marine incursion interpreted offshore (Souli/Nicoletto and horizon U; Fig. 3), which hints at brackish/lacustrine conditions before ~610 ka, and sea/lake level variations too subtle to produce marine terraces and markers in offshore sedimentation. Linear extrapolation using the uplift rate of the interpreted terraces suggests an age for the Klimenti Gilbert delta (Fig. 3) of 1.0±0.1 Ma. This slightly predates the age of 0.7±0.2 Ma marking the onset of the youngest and fastest deformation phase in the western Gulf of Corinth[11,34] dated with biostratigraphy, but is similar to the 1-2 Ma estimate for the oldest offshore sediments[12]. The most elevated Gilbert delta in the Gulf, the Mavro delta further west (Fig. 1), has been suggested to mark the onset of the modern and fast-extending Corinth Rift[10]. Compared to Klimenti, and comparing the inverted river drainage systems

associated with the formation of both deltas, Mavro has experienced more uplift (Fig. 3), indicating a slightly earlier onset of fault activity and/or higher average uplift rates.

We estimated the long-term slip rate and the uplift/subsidence (U:S) ratio by reconstructing the cross-section back to ~610 ka (Fig. 4). Palaeobathymetry in the Gulf ~610 ka is unknown, therefore in our reconstructions we apply a palaeobathymetry range from 800 m (todays maximum water depth) to 0 m, and correct for sediment compaction. The constant or slightly decelerating uplift rates onshore comparing New Corinth (II) to older terraces, and acceleration of subsidence rates offshore comparing H2 to older horizons (Supplementary Fig. 4), suggests a northward migration of fault activity (from Xylokastro to Lykoporia Fault, Fig. 3) affecting the most recent interglacial markers (~123-135 ka). Excluding those markers, and assuming most of the long-term deformation is related to the Xylokastro Fault, we estimate a long-term maximum subsidence rate of ~2.2-4 $mm \cdot yr^{-1}$ (Supplementary Fig. 4). Combining this with our long-term estimate of the maximum uplift rate from the marine terraces, and assuming the fault system is dipping 60° (Supplementary Fig. 5), we obtain a cumulative slip rate of 4.5-6.7 $mm \cdot yr^{-1}$ on the Xylokastro and Lykoporia faults and an U:S ratio of 1:1.2-2.4.

**Fault modelling**

The calculated U:S ratio is in disagreement with previous numerical fault models for Corinth that predict 2.7-3.5 times more subsidence than uplift for this fault system[10,35], motivating an updated approach by incorporating visco-elastic lithosphere-scale models at high resolution. We follow the principle of King et al.[36] that geological and geomorphic structures are the cumulative result of many earthquake cycles, and use a finite element model to solve for the surface displacements resulting from imposed normal slip on a planar fault in a simplified layered lithosphere. The fault plane runs through an elastic upper crust overlying a viscoelastic lower crust and upper mantle (Supplementary Fig. 7). We choose to reproduce the uplift and flexure pattern of the Old Corinth terrace shoreline (II) over 240 ka, because its deformed geometry is

particularly well-preserved and dated. We do not attempt to reproduce the depth to offshore markers, due to the uncertainty in palaeobathymetry at the time of their formation and effects of secondary faulting offshore, but we do show the range of likely depths for these markers (Fig. 5) defined by the estimated subsidence rates (Supplementary Fig. 4). Given the possible northward fault migration discussed in the previous section, we assume most of the deformation pre-dating ~135 ka is caused by the Xylokastro on- and offshore faults, and use the approximately perpendicular profile A-A' (Figs. 1, 3) as a reference section for our modeling, with the position of the onshore Xylokastro Fault as 0 m fault distance.

In Fig. 5a we show the parameters that have a major influence on the resulting deformation pattern. Compared to the reference model (M1), all these parameters influence the width of the uplifted zone, whereas all parameters but the upper crustal thickness influence the U:S ratio. The curvature of the footwall flexure is mainly influenced by the Young's Modulus of the upper crust and the viscosity of the lower crust, increasing in flexure with lower and higher values respectively. We show good fits to the data in Fig. 5b, using a 60° dipping fault as suggested from seismic data interpretation (Fig. 3; Supplementary Fig. 5), and a 10 km upper crustal thickness in agreement with the peak in microseismicity in this area of the Gulf (Supplementary Fig. 6). In our models we have used the range of possible slip rates from the previous section (4.5 – 6.7 $mm \cdot yr^{-1}$) and a regional uplift rate unrelated to rifting between 0-0.3 $mm \cdot yr^{-1}$ (see discussions in refs. [10,37]). Assuming the long-term Young's Modulus of the upper crust is comparable to short-term values, the lower crustal viscosity should be on the order of ~$10^{23}$ Pa·s to reproduce the correct curvature of the terraces, and an upper mantle viscosity between $5 \cdot 10^{21}$ and $2 \cdot 10^{22}$ Pa·s is required to match reasonable slip rates and regional uplift rates (M7, M8 in Fig. 5b; Supplementary Fig. 7). Increasing the lower crustal viscosity by an order of magnitude has a similar effect on the curvature of the flexure as decreasing the upper crustal Young's Modulus by an order of magnitude, but the latter has a stronger effect on the U:S ratio (M2 and M5; Fig. 5). Since the model becomes unstable with upper mantle viscosities lower

than ~$3 \cdot 10^{21}$ Pa·s, it is difficult to get good fits to the data with a Young's Modulus and lower crustal viscosity lower than the values for M9 (Fig. 5b). We attribute the mismatch in reproducing the offshore pattern to the presence of antithetic faults ~15 km north of the Xylokastro Fault (Figs. 3, 5), which modify the flexure pattern. Additional models with a 15 km upper crustal thickness, 50° fault, elastoplastic upper crust and non-linear (powerlaw) viscoelastic lower crust are discussed in the Supplementary Information (Supplementary Fig. 7 and Supplementary Table 1), but do not change our main results.

**Tectonic and rheological implications**

Our new revised slip rate estimate of 4.5-6.7 mm·yr$^{-1}$ based on both onshore and offshore data, is significantly lower than the previous estimate of 7.0-16 mm·yr$^{-1}$ for this fault system[9], determined when no well-constrained estimates of hanging wall subsidence existed. If we assume the fault system is dipping ~40° instead[18], the cumulative slip rate would be 6.0-9.0 mm·yr$^{-1}$, which is more similar but still has a much lower upper bound. This discrepancy in estimates shows that integrating on-and offshore data is essential for estimating slip rates of major fault structures, and thus for estimating potential earthquake recurrence and seismic hazard.

Compared to coseismic deformation, long-term patterns over many earthquake cycles tend to have a lower U:S ratio and broader wavelength of deformation due to postseismic relaxation processes of the deeper layers[36]. Few other studies have obtained long-term U:S ratios on crustal scale normal faults, but our estimate is in good agreement with the 1:1.2-2.2 estimate for the East Eliki Fault[38] (Fig. 1), and values of ~1:1-2.5 for normal faults in the Basin and Range[39]. The influence of the fault angle and upper crustal strength on this ratio has been pointed out by previous studies[10,36] and our study demonstrates that the rheology of the lower crust and upper mantle also play a major role in controlling the surface deformation pattern. Unlike those

studies, we do not require the long-term upper crustal strength to be lower than the short-term strength, or the effective elastic thickness to be smaller than the depth of the seismogenic layer. The best-fitting models for the terraces (Fig. 5b) have a lower crustal viscosity that is 2-20 times as high as the upper mantle viscosity. The relatively localised Moho rise (Fig. 5) in these models is a direct consequence of this viscosity contrast, and is in good agreement with local Moho geometry (Supplementary Fig. 6). Admittedly, the homogeneous viscosity layers in our models are simplifications and an important part of the postseismic relaxation could be taking place in the hotter, more ductile lowermost part of the crust, and much less in the strong upper portion of the upper mantle, the latter required in $10^6$-$10^8$ yr timescale models of rifting[40,41,42]. Even so, our results are in good agreement with compilations of postseismic relaxation studies on $10^0$-$10^3$ yr timescales that also show lower crustal viscosities to be generally higher than upper mantle viscosities[43,44], although ~1-3 orders of magnitude lower than our long-term viscosity estimates, which are more similar to Global Isostatic Adjustment modeling estimates on $10^3$-$10^4$ yr timescales[45]. It has been proposed that in tectonically active regions, high temperatures and fluids may locally weaken the upper mantle, in contrast to colder, stronger lithosphere away from those regions[44,46]. The Corinth Rift is located near the mantle wedge related to African plate subduction[47], and the tectonic history of the Aegean involves a complicated interplay of nappe stacking and backarc extension[48]. Within that framework hot and hydrous conditions may be expected, and could result in most of the postseismic relaxation taking place relatively deep, to allow the topographic signal of coseismic elastic flexure to be well maintained at the surface throughout many earthquake cycles. If all rifts worldwide are subjected to relatively high temperatures and hydrous conditions, our results may typify the rheology of rapid localised extension of continental lithosphere.

## Methods

**Marine terrace analysis**

To develop the DSM, we obtained tri-stereo Pleiades satellite images of 0.5m-resolution covering the terrace sequence between Xylokastro and Corinth. The open-source software MicMac[51,52] was used to create tie-points, orientate the images and calculate a 0.5m-resolution DSM, using ground control points at 0 m elevation for several locations along the coastline. To reduce the topographic effects of vegetation, crops and man-made structures, the DSM was downsampled to 2 m resolution (Fig. 2).

Mapping of the terraces (Figs. 1, 2 and Supplementary Fig. 1) was done semi-automatically using the surface classification model of Bowles and Cowgill[53], which combines the slope and roughness linearly to detect relatively low-slope smooth surfaces. Contours around those surfaces were drawn manually using a combination of satellite imagery, slope maps and hillshade images of the DSM. The slope of the Holocene seacliff was measured at 48 locations and its value ±1σ was used to estimate the horizontal and vertical position of the shoreline angles for ~700 paleocliffs with TerraceM[54,55] (Supplementary Fig. 2 and Supplementary Fig. 8). To reduce the influence of fluvial and gravitational erosion, we used the maximum topography of 100m-wide swath profiles perpendicular to the cliffs, the size preferred by Jara-Muñoz et al.[55]. All swath profile and shoreline angle locations are included as supplementary Google Earth and ESRI Shapefile data files. The terraces were correlated laterally using satellite imagery, mapview and profile view of shoreline angles in combination with a N130$^{o}$E coast-parallel swath stack[56] of 500 average elevations of swath profiles (Fig. 2d).

The uplift rate *U* for individual shoreline angles was calculated using $U = (H_T - H_{SL})/T$, where $H_T$ is the present elevation above the modern mean sea-level, $H_{SL}$ is the eustatic sea-level elevation for the time interval of terrace formation and T is the age of terrace formation.

Following Gallen et al.[57], standard errors SE were calculated using:

$$SE(u)^2 = u^2 \left( \left( \frac{{\sigma_H}^2}{(H_T - H_{SL})^2} \right) + \left( \frac{{\sigma_T}^2}{T^2} \right) \right) \quad (1)$$

where $\sigma_H$ is the combined uncertainty of shoreline angle elevation and eustatic sea-level correction, and $\sigma_T$ is the uncertainty in age of terrace formation. For the eustatic sea-level highstands MIS 5e, MIS 7e, MIS 9e and MIS 11c, correlated to the New Corinth (II), Old Corinth (II), Temple (II) and Laliotis terraces, we used ages of 123.5±8.5 ka, 240±6 ka, 326±9 ka and 409±16 ka[58], and sea-level corrections of 5.5±3.5 m, 0.5±3.5 m, 2.5±5.5 m and 5±8 m[59] respectively. The uplift rate at the onshore Xylokastro Fault was estimated by combining the New Corinth (II), Old Corinth (II), Temple (II) and Laliotis uplift rates and extrapolating a best fitting quadratic curve with Matlab® (Supplementary Fig. 4). A critical $\chi^2$ test was done to confirm that the residuals follow a Gaussian distribution and the uplift rate dataset is well described by the curve[60], which was the case when excluding the New Corinth (II) terrace, but not when including that terrace.

**Constructing cross-section and evolution model**

We depth-converted the multi-channel seismic section L35[18] using the velocity model of Taylor et al.[18], and adopted the interpretation of faults and seismic horizons from Nixon et al.[33] (Supplementary Fig. 5). The shoreline angles were reprojected on a profile of the same orientation as the seismic section, approximately perpendicular to the on- and offshore Xylokastro Fault (Fig. 1 and Fig. 3). To combine the terraces with topsets of the overlying Klimenti Delta the maximum elevation of a 4-km wide, N025E oriented swath profile was also reprojected along the same line (Fig. 1). The river profile of the inverted Safenatos River and the windgap-connected trunk of the Trikalitikos river were merged together, and horizontally scaled to have the windgap at the correct location within the cross-section and the river outlet at the

coastline. Best-fitting quadratic curves for the New Corinth (II), Old Corinth (II), Temple (II) and Laliotis terraces were extracted with Matlab®. The Laliotis curve, assuming an age of 409 ka and a eustatic sea-level correction of +5 m, was extrapolated linearly to estimate total uplift at 605 ka and 1050 ka, approximately corresponding to the sea-level highstand following the oldest marine incursion interpreted offshore (Fig. 3b) and the age to match the position of the Klimenti Delta overlying the terrace sequence (Fig. 3a). The sill depth is chosen at 62 m[29], and for simplicity chosen as constant through time. Given the fast rate of sea-level rise before major interglacial highstands, uncertainty in sill depth does not change the age of the interpreted offshore horizons much, nor does the depth-uncertainty in the sea-level curve. We chose to display the sea-level curve of Bates et al.[50] since it is the most recent curve that we are aware of covering >610 ka that is accounting for global observations of uplifted paleoshorelines, and use their equatorial Pacific curve since they use it as reference curve. For the background topography comprising the Mavro Gilbert delta (Fig. 3c) we used a 4-km wide swath profile along the same orientation as A-A'.

In the evolution model (Fig. 4) the paleodepth of the Corinth Gulf at 605 ka was chosen at 400 m as an average of two end-member scenarios at which seismic horizon U would represent the sea-level at 0 m, or the local sea bottom at its present-day depth of ~800 m. Sea/lake deepening was assumed to be constant between 605 ka and present, and sediments were decompacted using a porosity-depth relationship for calcareous sediments from Nixon et al.[33], based on experimental data[61]. A subsidence rate over the past ~610 ka was calculated by taking the current depth of seismic horizon U of ~2480 m depth, substracting 0-800 m for the sea/lake paleodepth and 415-312 m due to compaction of the sediments below the U horizon. The same principle was applied for every individual horizon in Supplementary Fig. 4, and used for the error margins in Fig. 5 and Supplementary Fig. 7. Since reconstruction of the maximum swath profile topography from Fig. 3 should be relatively insensitive to river incision, we did not take into account onshore erosion processes in Fig. 4.

**Fault modelling**

For the fault modelling we used PyLith[62], an open-source finite element code for dynamic and quasi-static simulations of crustal deformation. We used a starting model with a 10 km upper crustal thickness, adopting the peak in microseismicity depth (Supplementary Fig. 6) around the cross-section of Fig. 3, and a 35 km crustal thickness following Moho depth estimates from Ps receiver functions[63] and tomographic inversion of PmP reflection times[64]. Listric and biplanar fault geometries were excluded from our models, since they are not expected to give the significant footwall uplift that our data suggests[65]. For model simplicity we exclude erosion and sedimentation processes, to which previous numerical models were relatively insensitive[10]. We used 2.5-m slip earthquakes with a recurrence time of 500 years, following our range of estimated long-term slip rates, and roughly in agreement with the recurrence times for major earthquakes inferred from offshore paleoseismology[66]. The models have uniform slip until the base of the upper crust, linearly decreasing to 0 m slip at 12 km depth to avoid extreme boundary effects at the fault tip. Sensitivity tests suggest the models are insensitive to the recurrence time if the slip rate is the same, and the ground surface pattern for different slip rates can be approximated by linear inter- or extrapolation of the displacement vector after the model run (Supplementary Fig. 7). For the models with an elastoplastic upper crust (Supplementary Fig. 7) we used the plastic parameters from Cianetti et al.[35] and for the models with a non-linear (powerlaw) viscoelastic lower crust we used the quartz flow law from Gleason and Tullis[67]. In all model runs we included gravitational body forces and used a finite strain formulation.

**References**

1. Kusznir, N. J. & Park, R. G. The extensional strength of the continental lithosphere: its dependence on geothermal gradient, and crustal composition and thickness. *Geological*

*Society, London, Special Publications* **28,** 35–52 (1987).

2. King, G. C. P. *et al.* The evolution of the Gulf of Corinth (Greece): an aftershock study of the 1981 earthquakes. *Geophys. J. Int.* **80,** 677–693 (1985).
3. Nishimura, T. Rheology of the lithosphere inferred from postseismic uplift following the 1959 Hebgen Lake earthquake. *J. Geophys. Res.* **108,** (2003).
4. Gourmelen, N. & Amelung, F. Postseismic mantle relaxation in the Central Nevada Seismic Belt. *Science* **310,** 1473–1476 (2005).
5. Lambotte, S. *et al.* Reassessment of the rifting process in the Western Corinth Rift from relocated seismicity. *Geophys. J. Int.* **197,** 1822–1844 (2014).
6. Buck, W. R. Flexural rotation of normal faults. *Tectonics* **7,** 959–973 (1988).
7. Jackson, J. A. & White, N. J. Normal faulting in the upper continental crust: observations from regions of active extension. *J. Struct. Geol.* **11,** 15–36 (1989).
8. Watts, A. B. & Burov, E. B. Lithospheric strength and its relationship to the elastic and seismogenic layer thickness. *Earth Planet. Sci. Lett.* **213,** 113–131 (2003).
9. Huismans, R. & Beaumont, C. Depth-dependent extension, two-stage breakup and cratonic underplating at rifted margins. *Nature* **473,** 74–78 (2011).
10. Armijo, R., Meyer, B., King, G. C. P., Rigo, A. & Papanastassiou, D. Quaternary evolution of the Corinth Rift and its implications for the Late Cenozoic evolution of the Aegean. *Geophys. J. Int.* **126,** 11–53 (1996).
11. Rohais, S., Eschard, R., Ford, M., Guillocheau, F. & Moretti, I. Stratigraphic architecture of the Plio-Pleistocene infill of the Corinth Rift: Implications for its structural evolution. *Tectonophysics* **440,** 5–28 (2007).
12. Bell, R. E. *et al.* Fault architecture, basin structure and evolution of the Gulf of Corinth Rift, central Greece. *Basin Res.* **21,** 824–855 (2009).
13. Raymo, M. E., Oppo, D. W. & Curry, W. The Mid-Pleistocene climate transition: A deep sea

carbon isotopic perspective. *Paleoceanography* **12,** 546–559 (1997).

14. Medina-Elizalde, M. & Lea, D. W. The mid-Pleistocene transition in the tropical Pacific. *Science* **310,** 1009–1012 (2005).
15. Roberts, G. P. *et al.* Localization of Quaternary slip rates in an active rift in $10^5$ years: An example from central Greece constrained by $^{234}U$-$^{230}Th$ coral dates from uplifted paleoshorelines. *J. Geophys. Res.* **114,** (2009).
16. Heezen, B. C., Ewing, M. & Johnson, G. L. The Gulf of Corinth floor. *Deep Sea Research and Oceanographic Abstracts* **13,** 381–411 (1966).
17. Collier, R. E. L. L. Eustatic and tectonic controls upon Quaternary coastal sedimentation in the Corinth Basin, Greece. *J. Geol. Soc. London* **147,** 301–314 (1990).
18. Taylor, B. *et al.* The structures, stratigraphy and evolution of the Gulf of Corinth rift, Greece. *Geophys. J. Int.* **185,** 1189–1219 (2011).
19. Dufaure, J.-J. & Zamanis, A. Un vieux problème géomorphologique : les niveaux bordiers au sud du Golfe de Corinthe (An old geomorphological problem : the levels developed on the southern border of the Gulf of Corinth). *Bulletin de l'Association de géographes français* **56,** 341–350 (1979).
20. Keraudren, B. & Sorel, D. The terraces of Corinth (Greece) — A detailed record of eustatic sea-level variations during the last 500,000 years. *Mar. Geol.* **77,** 99–107 (1987).
21. Lajoie, K. R. Coastal tectonics. *Active tectonics* (1986).
22. Scott, A. & Pinter, N. Extraction of Coastal Terraces and Shoreline-Angle Elevations from Digital Terrain Models, Santa Cruz and Anacapa Islands, California. *Phys. Geogr.* **24,** 271–294 (2003).
23. Pedoja, K. *et al.* Coastal staircase sequences reflecting sea-level oscillations and tectonic uplift during the Quaternary and Neogene. *Earth-Sci. Rev.* **132,** 13–38 (2014/5).
24. Caputo, R. Sea-level curves: Perplexities of an end-user in morphotectonic applications. *Glob. Planet. Change* **57,** 417–423 (2007).

25. Collier, R. E. L., Leeder, M. R., Rowe, P. J. & Atkinson, T. C. Rates of tectonic uplift in the Corinth and Megara Basins, central Greece. *Tectonics* **11,** 1159–1167 (1992).
26. Dia, A. N., Cohen, A. S., O'Nions, R. K. & Jackson, J. A. Rates of uplift investigated through 230Th dating in the Gulf of Corinth (Greece). *Chem. Geol.* **138,** 171–184 (1997).
27. Leeder, M. R. *et al.* Normal faulting and crustal deformation, Alkyonides Gulf and Perachora peninsula, eastern Gulf of Corinth rift, Greece. *J. Geol. Soc. London* **162,** 549–561 (2005).
28. Pierini, F., Demarchi, B., Turner, J. & Penkman, K. Pecten as a new substrate for IcPD dating: The quaternary raised beaches in the Gulf of Corinth, Greece. *Quat. Geochronol.* **31,** 40–52 (2016/2).
29. Perissoratis, C., Piper, D. J. W. & Lykousis, V. Alternating marine and lacustrine sedimentation during late Quaternary in the Gulf of Corinth rift basin, central Greece. *Mar. Geol.* **167,** 391–411 (2000).
30. Palyvos, N. *et al.* Geomorphological, stratigraphic and geochronological evidence of fast Pleistocene coastal uplift in the westernmost part of the Corinth Gulf Rift (Greece). *Geol. J.* **45,** 78–104 (2010).
31. Moretti, I. *et al.* Sedimentation and subsidence rate in the Gulf of Corinth: what we learn from the Marion Dufresne's long-piston coring. *C. R. Geosci.* **336,** 291–299 (2004).
32. Sachpazi, M., Clément, C., Laigle, M., Hirn, A. & Roussos, N. Rift structure, evolution, and earthquakes in the Gulf of Corinth, from reflection seismic images. *Earth Planet. Sci. Lett.* **216,** 243–257 (2003).
33. Nixon, C. W. *et al.* Rapid spatiotemporal variations in rift structure during development of the Corinth Rift, central Greece. *Tectonics* **35,** 1225–1248 (2016).
34. Ford, M., Hemelsdaël, R., Mancini, M. & Palyvos, N. Rift migration and lateral propagation: evolution of normal faults and sediment-routing systems of the western Corinth rift (Greece). *Geological Society, London, Special Publications* SP439.15 (2016).

35. Cianetti, S., Tinti, E., Giunchi, C. & Cocco, M. Modelling deformation rates in the western Gulf of Corinth: rheological constraints. *Geophys. J. Int.* **174,** 749–757 (2008).
36. King, G. C. P., Stein, R. S. & Rundle, J. B. The Growth of Geological Structures by Repeated Earthquakes 1. Conceptual Framework. *J. Geophys. Res.* **93,** 13307–13318 (1988).
37. Turner, J. A. *et al.* Testing rival tectonic uplift models for the Lechaion Gulf in the Gulf of Corinth rift. *J. Geol. Soc. London* **167,** 1237–1250 (2010).
38. McNeill, L. C., Collier, R. E. L., De Martini, P. M., Pantosti, D. & D'Addezio, G. Recent history of the Eastern Eliki Fault, Gulf of Corinth: geomorphology, palaeoseismology and impact on palaeoenvironments. *Geophys. J. Int.* **161,** 154–166 (2005).
39. King, G. C. P., Stein, R. S. & Rundle, J. The growth of geological structures by repeated earthquakes, 2: Field examples of continental dip-slip faults. *J. Geophys. Res.* **93,** 13319–13331 (1988).
40. Riva, R. E. M. & Govers, R. Relating viscosities from postseismic relaxation to a realistic viscosity structure for the lithosphere. *Geophys. J. Int.* **176,** 614–624 (2009).
41. Hines, T. T. & Hetland, E. A. Bias in estimates of lithosphere viscosity from interseismic deformation. *Geophys. Res. Lett.* **40,** 4260–4265 (2013).
42. Burov, E. B. & Watts, A. B. The long-term strength of continental lithosphere:' jelly sandwich' or' crème brûlée'? *GSA Today* **16,** 4 (2006).
43. Thatcher, W. & Pollitz, F. F. Temporal evolution of continental lithospheric strength in actively deforming regions. *GSA Today* **18,** 4 (2008).
44. Wright, T. J., Elliott, J. R., Wang, H. & Ryder, I. Earthquake cycle deformation and the Moho: Implications for the rheology of continental lithosphere. *Tectonophysics* **609,** 504–523 (2013).
45. Caron, L., Métivier, L., Greff-Lefftz, M., Fleitout, L. & Rouby, H. Inverting Glacial Isostatic Adjustment signal using Bayesian framework and two linearly relaxing rheologies.

*Geophys. J. Int.* **209,** 1126–1147 (2017).

46. Bürgmann, R. & Dresen, G. Rheology of the Lower Crust and Upper Mantle: Evidence from Rock Mechanics, Geodesy, and Field Observations. *Annual Review of Earth and Planetary* (2008). doi:10.1146/annurev.earth.36.031207.124326
47. Suckale, J. *et al.* High-resolution seismic imaging of the western Hellenic subduction zone using teleseismic scattered waves. *Geophys. J. Int.* **178,** 775–791 (2009).
48. Jolivet, L. & Brun, J.-P. Cenozoic geodynamic evolution of the Aegean. *Int. J. Earth Sci.* **99,** 109–138 (2010).
49. De Martini, P. M. *et al.* Slip rates of the Aigion and Eliki Faults from uplifted marine terraces, Corinth Gulf, Greece. *C. R. Geosci.* **336,** 325–334 (2004).
50. Bates, S. L., Siddall, M. & Waelbroeck, C. Hydrographic variations in deep ocean temperature over the mid-Pleistocene transition. *Quat. Sci. Rev.* **88,** 147–158 (2014).

**References Methods**

51. Rosu, A.-M., Pierrot-Deseilligny, M., Delorme, A., Binet, R. & Klinger, Y. Measurement of ground displacement from optical satellite image correlation using the free open-source software MicMac. *ISPRS J. Photogramm. Remote Sens.* **100,** 48–59 (2015/2).
52. Rupnika, E., Deseillignya, M. P., Delorme, A. & Klinger, Y. Refined satellite image orientation in the free open-source photogrammetric tools Apero/Micmac. *ISPRS Annals of Photogrammetry, Remote Sensing & Spatial Information Sciences* **3,** (2016).
53. Bowles, C. J. & Cowgill, E. Discovering marine terraces using airborne LiDAR along the Mendocino-Sonoma coast, northern California. *Geosphere* **8,** 386–402 (2012).
54. Gelder, D. *et al.* Corinth terraces re-visited: Improved paleoshoreline determination using Pleiades-DEMs. *Geotectonic Research* **97,** 12–14 (2015).
55. Jara-Muñoz, J., Melnick, D. & Strecker, M. R. TerraceM: A MATLAB® tool to analyze marine and lacustrine terraces using high-resolution topography. *Geosphere* **12,** 176–195

(2016).

56. Armijo, R., Lacassin, R., Coudurier-Curveur, A. & Carrizo, D. Coupled tectonic evolution of Andean orogeny and global climate. *Earth-Sci. Rev.* **143,** 1–35 (2015/4).
57. Gallen, S. F. *et al.* Active simultaneous uplift and margin-normal extension in a forearc high, Crete, Greece. *Earth Planet. Sci. Lett.* **398,** 11–24 (2014).
58. Masson-Delmotte, V. *et al.* EPICA Dome C record of glacial and interglacial intensities. *Quat. Sci. Rev.* **29,** 113–128 (2010/1).
59. Murray-Wallace, C. V. & Woodroffe, C. D. *Quaternary Sea-Level Changes: A Global Perspective*. (Cambridge University Press, 2014).
60. Trauth, M. H. *MATLAB® Recipes for Earth Sciences:* (Springer Berlin Heidelberg, 2015).
61. Goldhammer, R. K. Compaction and decompaction algorithms for sedimentary carbonates. *J. Sediment. Res.* **67,** (1997).
62. Aagaard, B., Williams, C. & Knepley, M. PyLith: A finite-element code for modeling quasi-static and dynamic crustal deformation. *Eos Trans. AGU* **89,** (2008).
63. Pearce, F. D. (Seismic imaging of the western Hellenic subduction zone : the relationship between slab composition, retreat rate, and overriding lithosphere genesis. (PhD thesis Massachusetts Institute of Technology, 2015).
64. Zelt, B. C., Taylor, B., Sachpazi, M. & Hirn, A. Crustal velocity and Moho structure beneath the Gulf of Corinth, Greece. *Geophys. J. Int.* **162,** 257–268 (2005).
65. Resor, P. G. & Pollard, D. D. Reverse drag revisited: Why footwall deformation may be the key to inferring listric fault geometry. *J. Struct. Geol.* **41,** 98–109 (2012).
66. Campos, C. *et al.* Deciphering hemipelagites from homogenites through anisotropy of magnetic susceptibility. Paleoseismic implications (Sea of Marmara and Gulf of Corinth). *Sediment. Geol.* **292,** 1–14 (2013).
67. Gleason, G. C. & Tullis, J. A flow law for dislocation creep of quartz aggregates determined with the molten salt cell. *Tectonophysics* **247,** 1–23 (1995).

**Acknowledgements**

The research leading to these results has received funding from the People Programme (Marie Curie Actions) of the European Union's Seventh Framework Programme under the ITN project ALErT (Grant FP7-PEOPLE-2013-ITN number 607996) and by the ISIS program of CNES. The authors thank Arthur Delorme for his technical assistance in producing the DSMs. Numerical computations for the DSM were performed on the S-CAPAD platform, Institut de Physique du Globe de Paris (IPGP), France. Seismic reflection data from EW0108 is available from the Marine Geoscience Data System.

**Author contributions**

G.D.G., D.F.-B. and R.L. designed the study, D.F.-B. produced the map and stacked swath, G.D.G. and R.A. mapped the marine terraces and performed their analysis together with D.M. and J.J.-M. R.E.B. depth-converted the seismic section, G.D.G. and G.D. performed the numerical fault modeling. All authors discussed the results at different stages of the process. G.D.G. wrote the paper with contributions and edits from all other authors.

**Competing Financial Interests statement**

The authors declare no competing financial interests.

**Data availability**

The Pleiades satellite imagery was obtained through the ISIS and Tosca programs of the Centre National d'Etudes Spatiales (CNES, France) under an academic license and is not for open distribution. On request, we'll provide the DSM calculated from this imagery to any academic researcher who gets approval from CNES (contact isis-pleiades@cnes.fr for quoting this paper,

and with lacassin@ipgp.fr in copy). The other data that support the findings of this study are available within the publication, referenced studies and/or from the corresponding author on request.

**Figures**

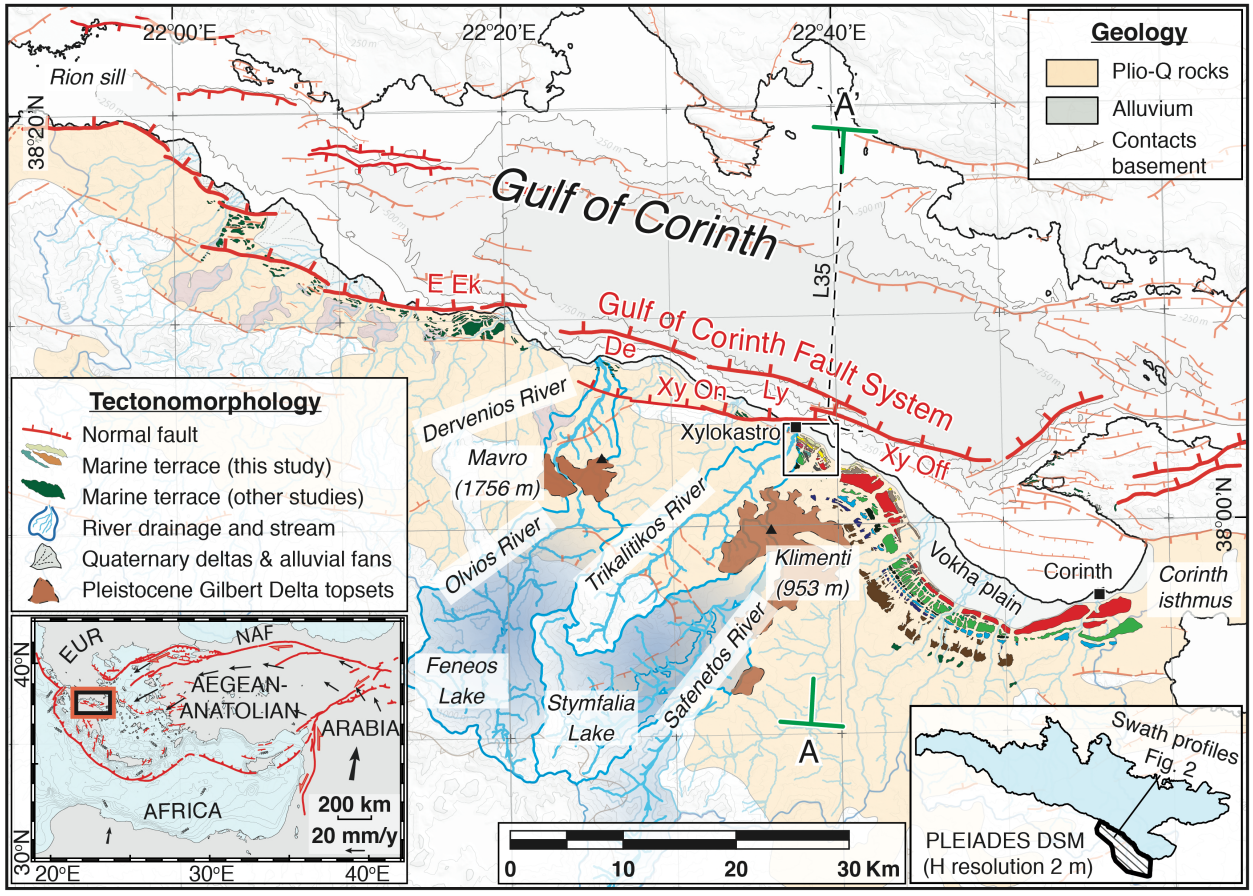


**Figure 1: Active tectonics in the Gulf of Corinth.** Solid box outlines location of Fig. 2, and A-A' indicates cross-section location for Fig. 3. Faults mentioned in the text are the East Eliki (E Ek), Derveni (De), Lykoporia (Ly) and Xylokastro on- and offshore faults (Xy On and Xy Off). Marine terraces from other studies have been adopted from refs [10,15,49]. Map was made using MAPublisher® version 9.8 (http://www.avenza.com/help/mapublisher/9.8/).

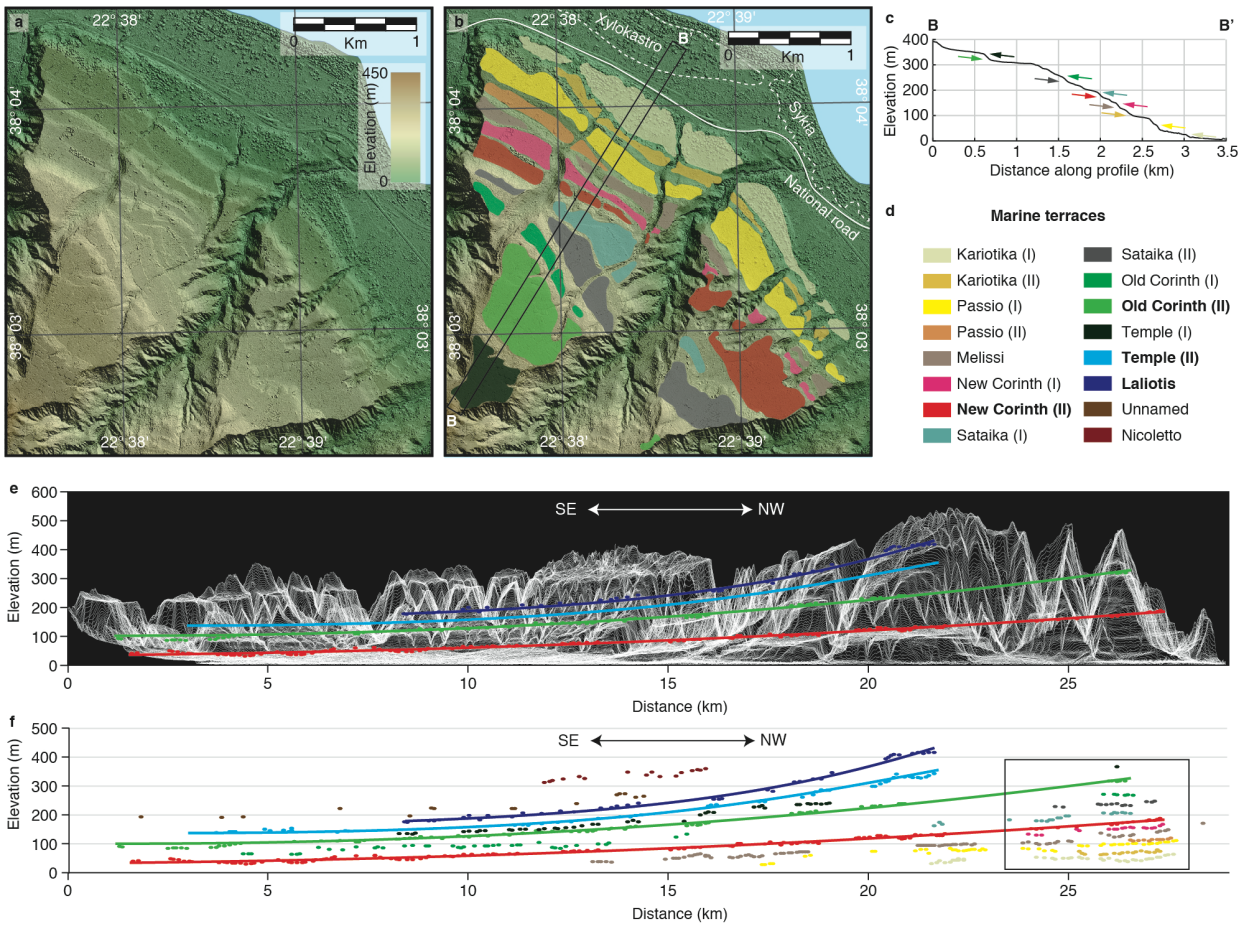


**Figure 2: Detail of marine terraces on Pleiades DSM (a)** Coloured hillshade DSM without interpretation, location given by inset in Fig. 1. **(b)** Same DSM with contouring of marine terraces. **(c)** Average swath topography through marine terraces levels, location given by inset in **b**. **(d)** Marine terrace legend, bold terraces are highlighted in **e**, **f** and Fig. 3. **(e)** Topography "view" parallel to the coast derived using stacked swath profiles with the shoreline angles and best fitting quadratic curves for the New Corinth (I), Old Corinth (II), Temple (II) and Laliotis terraces. **(f)** All determined shoreline angles along the same profile. Box shows location of **a** and **b**. Maps were made using MAPublisher® version 9.8 (http://www.avenza.com/help/mapublisher/9.8/).

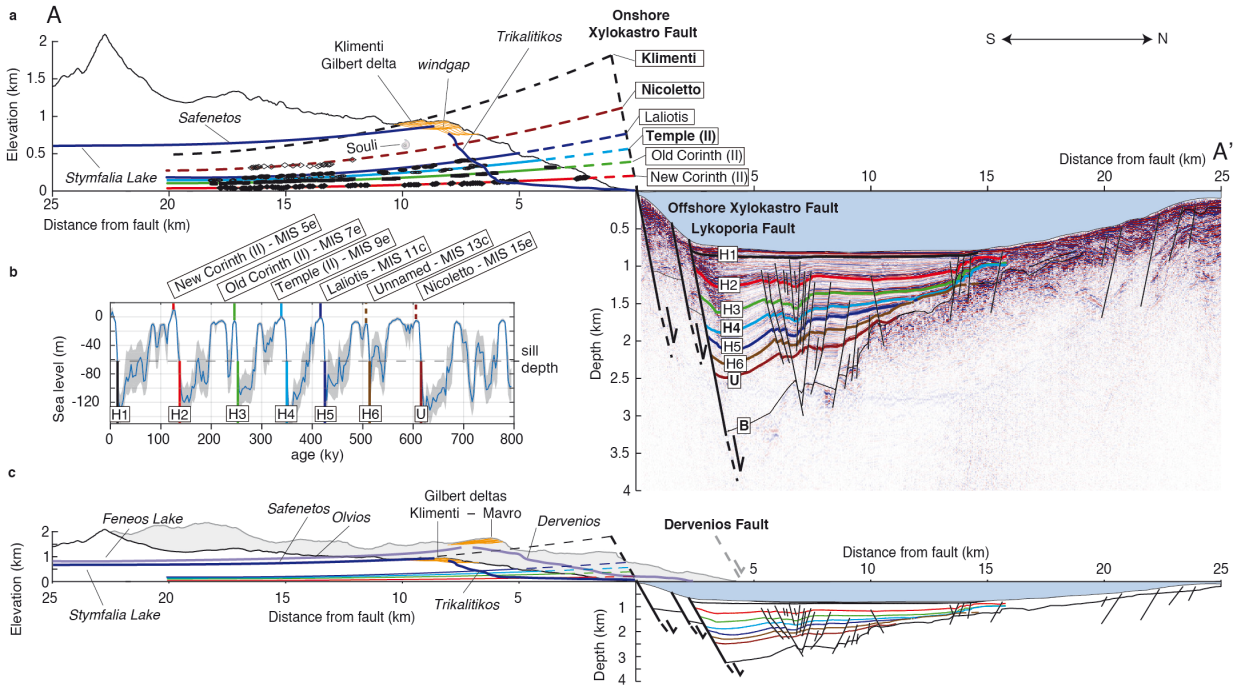


**Figure 3: Combined on-offshore cross-section through Corinth Rift. (a)** Cross-section with 3x vertical exaggeration, showing maximum topography of a 4-km wide swath profile across the Xylokastro terraces (Fig. 2a, b) and top of the Klimenti Gilbert Delta (Fig. 1), shoreline angles of terraces assigned to major sea-level highstands with best-fitting quadratic curves and part of the Trikalitikos-Safenetos river system, all reprojected on line A-A' of Fig. 1. Offshore seismic section is the interpretation of Nixon et al.[33] on the depth-converted line L35 from Taylor et al.[18]. **(b)** Inferred ages of marine terrace levels and offshore seismic horizons plotted on the Pacific sea-level curve of Bates et al.[50] **(c)** Main features of **a** without vertical exaggeration, and including the maximum topography of a 4-km wide swath profile parallel to A-A' across the Mavro Gilbert Delta.

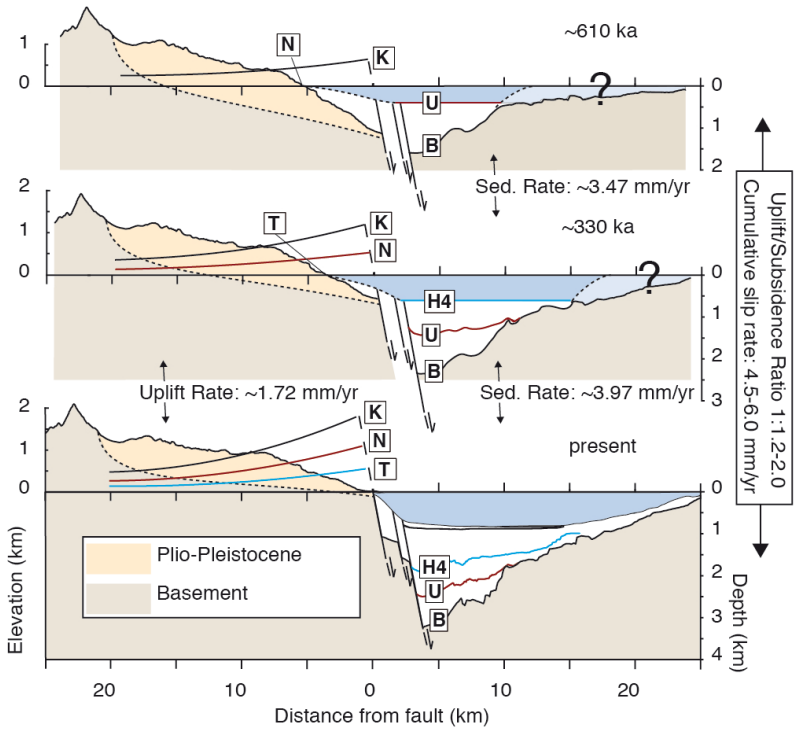


**Figure 4: Schematic geologic restoration.** The bold-labelled terraces and seismic horizons from Fig. 3 rotated back to horizontal, with the same rotation applied to the topo-bathymetry, accounting for sediment compaction.

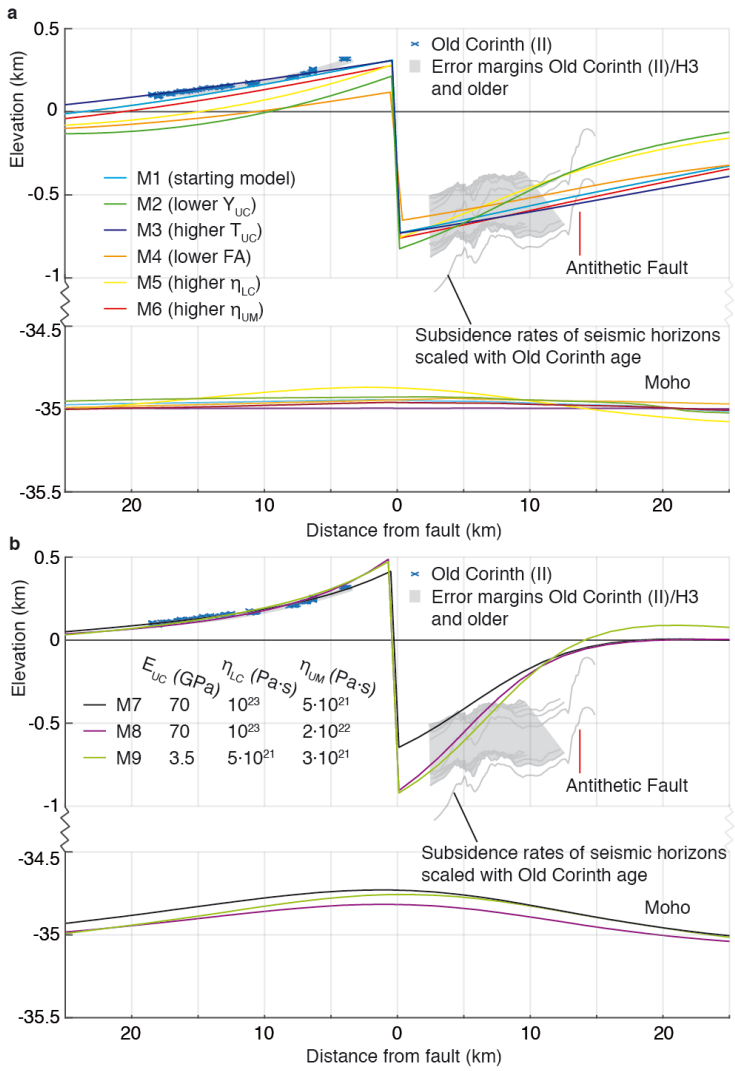


**Figure 5: Fault modelling results. (a)** Sensitivity tests for the different model parameters compared to the Old Corinth (II) terrace. $E_{UC}$ = Young's Modulus of upper crust, $T_{UC}$ = thickness of upper crust, FA = fault dip angle, $\eta_{LC}$ = viscosity of lower crust, $\eta_{UM}$ = viscosity of upper mantle. **(b)** Best-fitting models, which reproduce fault flexure by a relatively high viscosity lower crust (models 7 and 8) or an upper crust with relatively low Young's Modulus (model 9). Model 7 has a slip rate of 4.5 mm·yr$^{-1}$ and 0 mm·yr$^{-1}$ of regional uplift rate, models 8 and 9 have a slip rate of 6.7 mm·yr$^{-1}$ and 0.3 mm·yr$^{-1}$ of regional uplift rate.

# Supplementary Information

**(Fault flexure and lithosphere rheology set from climate cycles record in the Corinth Rift**

Gino de Gelder[1*], David Fernández-Blanco[1], Daniel Melnick[2,3], Guillaume Duclaux[4], Rebecca E. Bell[5], Julius Jara-Muñoz[2], Rolando Armijo[1] and Robin Lacassin[1])

This file includes 7 supplementary figures, and 1 supplementary table. Supplementary Figure 8 is a data repository and can be retrieved with this link:

https://figshare.com/s/bff68e81da9c540ae29f

Additionally, we share a georeferenced hillshade image and slope map of the 2 m-resolution Digital Surface Model that was developed from Pleiades satellite imagery, and formed the basis for marine terrace analysis. This image can be retrieved with these links:

https://figshare.com/s/05d6610458391e9da3d7(hillshade image)

https://figshare.com/s/a50519854408656e2532(slope map)

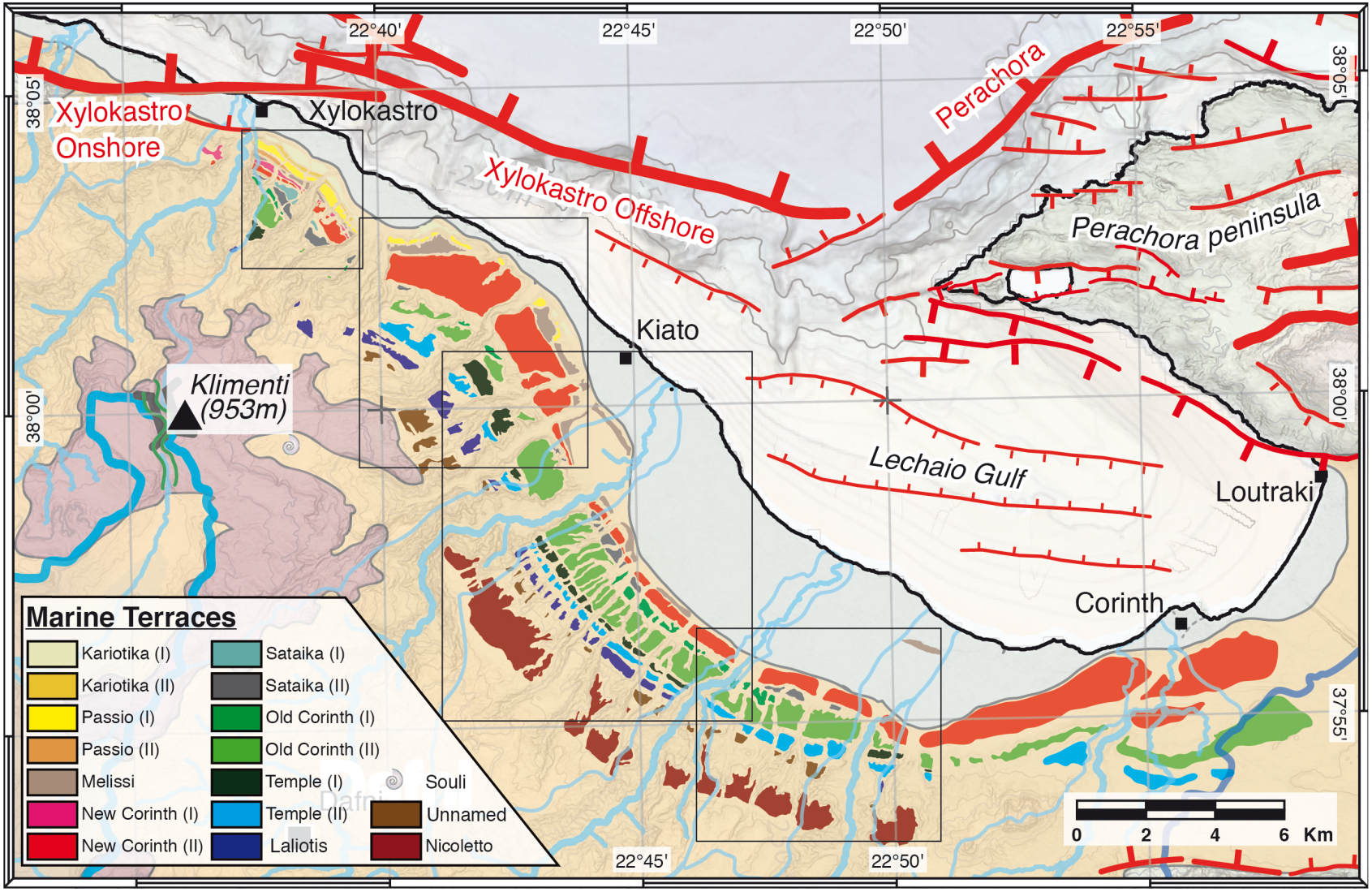
22°40'
22°45'
22°50'
22°55'
38°05'
38°00'
37°55'
Xylokastro Onshore
Xylokastro
Xylokastro Offshore
Perachora
Perachora peninsula
Kiato
Klimenti (953m)
Lechaio Gulf
Loutraki
Corinth
Marine Terraces
Kariotika (I)
Kariotika (II)
Passio (I)
Passio (II)
Melissi
New Corinth (I)
New Corinth (II)
Sataika (I)
Sataika (II)
Old Corinth (I)
Old Corinth (II)
Temple (I)
Temple (II)
Laliotis
Souli
Unnamed
Nicoletto
0 2 4 6 Km

**Supplementary Figure 1 (previous page)**: **Marine terraces between Xylokastro and Corinth.** Based on detailed mapping with Pleiades DSM, with coloring and names modified from Armijo et al.[9]. Boxes indicate location of maps in Supplementary Fig. 8. Map was made using MAPublisher® version 9.8 (http://www.avenza.com/help/mapublisher/9.8/).

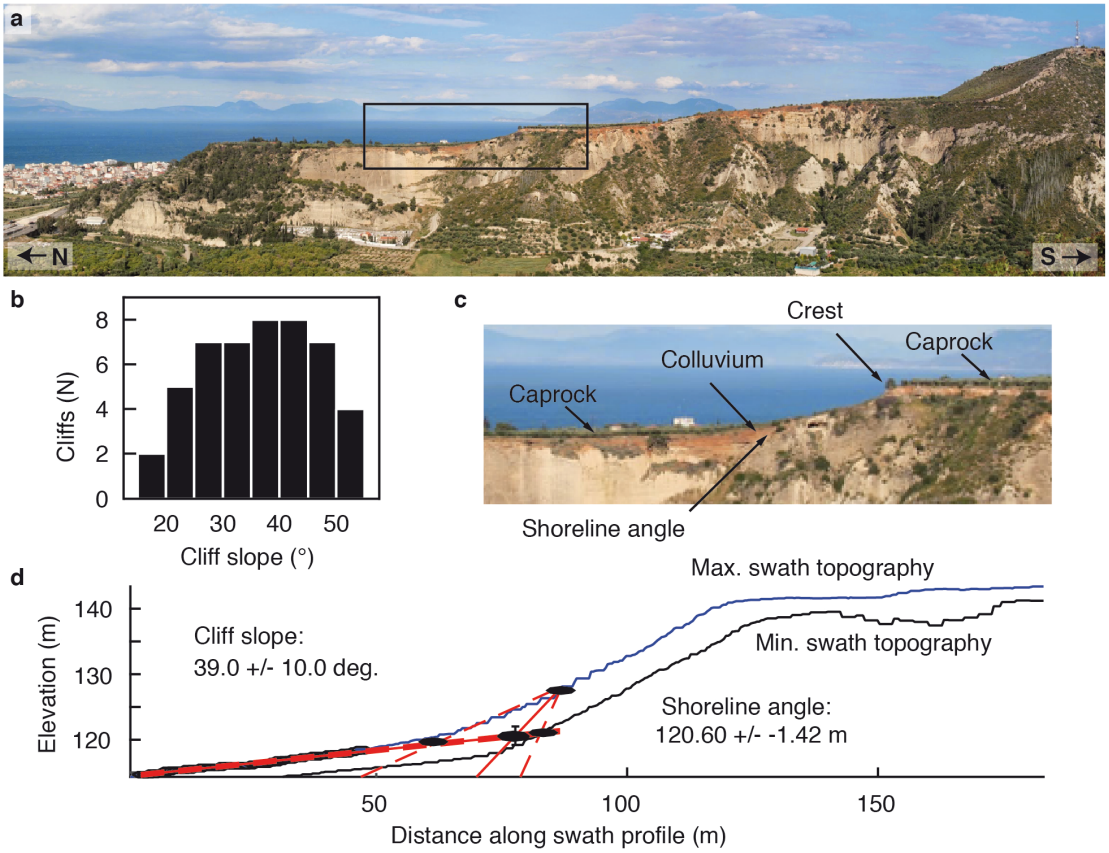


**Supplementary Figure 2: Shoreline angle determination. (a)** View of terraces near Xylokastro **(b)** Histogram of Holocene cliff slope measurements **(c)** Detail of terrace morphology from inset in **a (d)** Example of TerraceM shoreline angle analysis

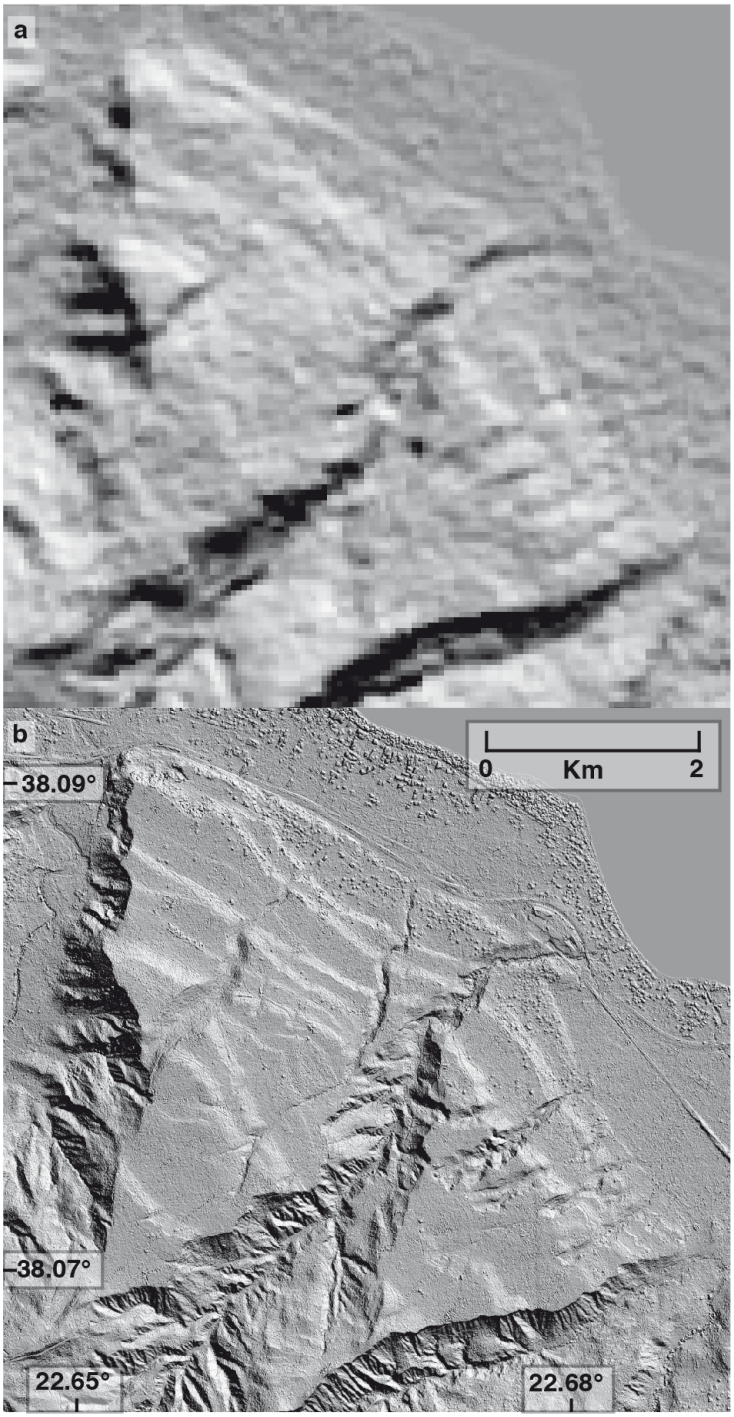


**Supplementary Figure 3: Digital Elevation Model comparison.** Hillshade images from **(a)** an ASTER DEM of 30m resolution and **(b)** a Pleiades DSM of 2m resolution.

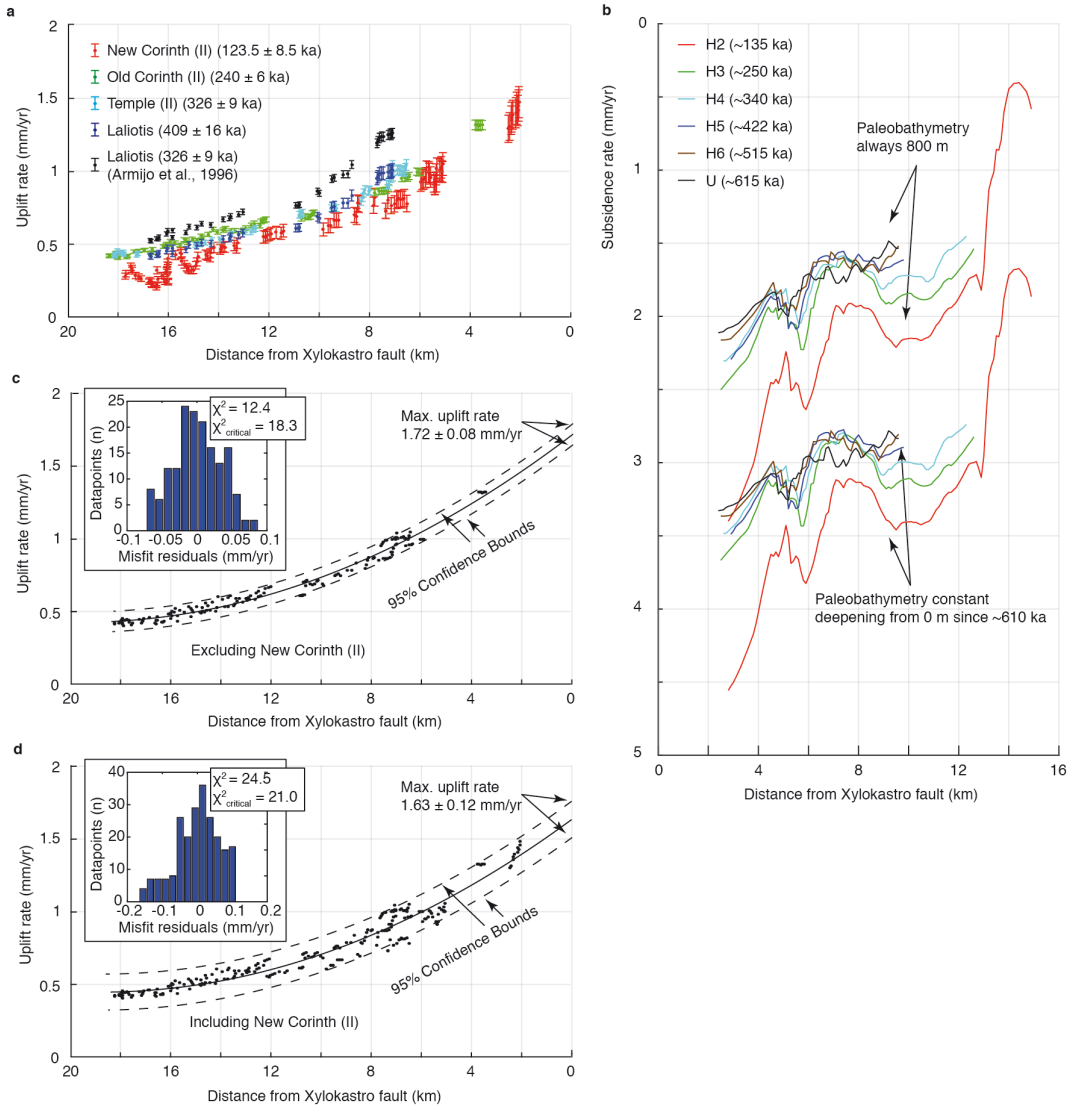


**Supplementary Figure 4: Uplift/subsidence rates. (a)** Estimated uplift rates for selected shoreline angles from Fig. 2f **(b)** Estimated subsidence rates for seismic horizons in Fig. 3 **(c)** Old Corinth (II), Temple (II) and Laliotis uplift rates grouped together and best fitting quadratic curve, including 95% confidence bounds, extrapolated to estimate uplift rate near fault. Inset shows histogram of residuals and values for critical $\chi^2$ test. **(d)** Same as **c**, but including the New Corinth (II) terrace

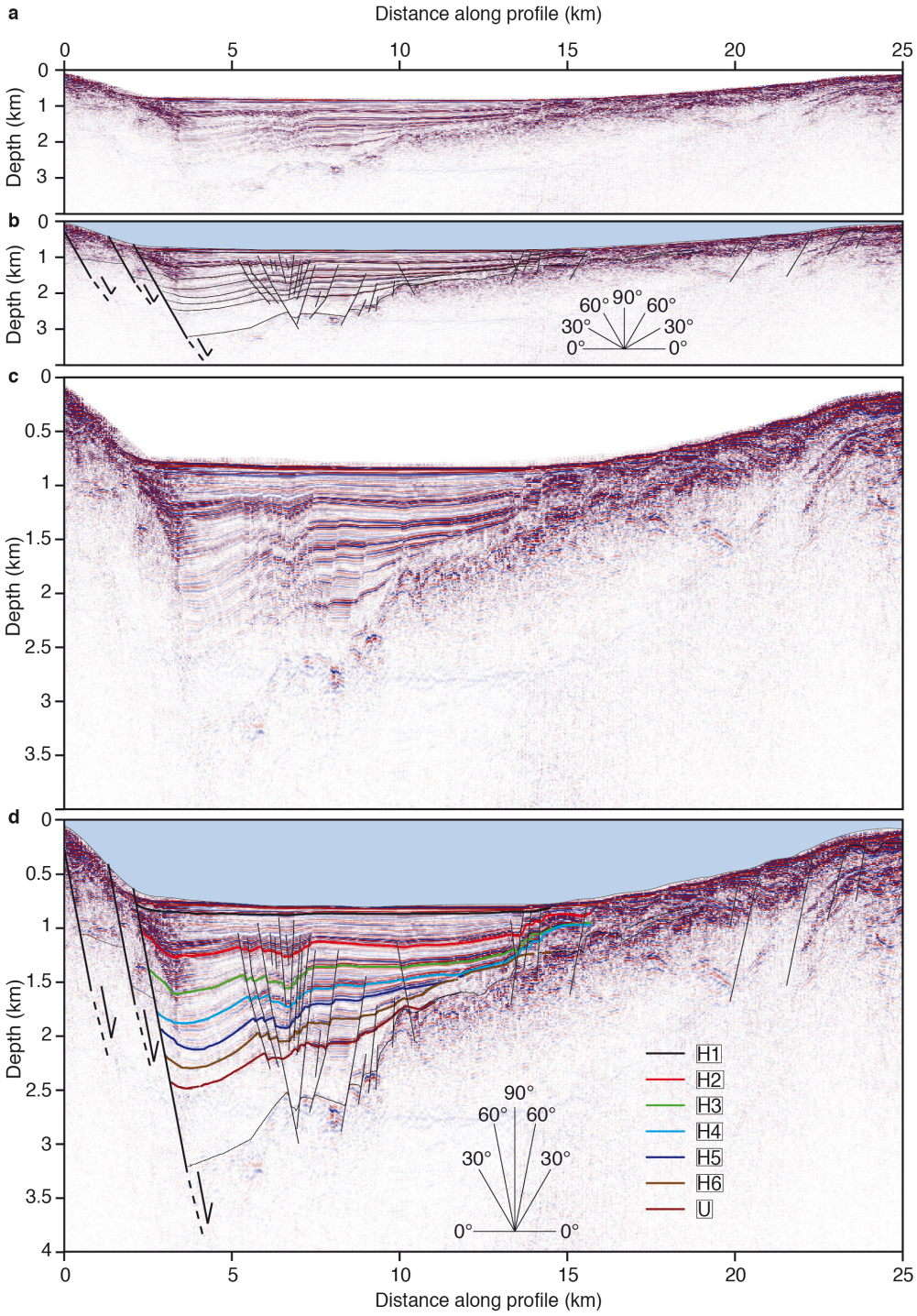


**Supplementary Figure 5: Converted offshore seismic section of line L35**[13]**. (a)** Without interpretation and vertical exaggeration **(b)** With interpretation from Nixon et al.[34] and without vertical exaggeration **(c)** Without interpretation and with 3x vertical exaggeration **(d)** With interpretation from Nixon et al.[34] and 3x vertical exaggeration.

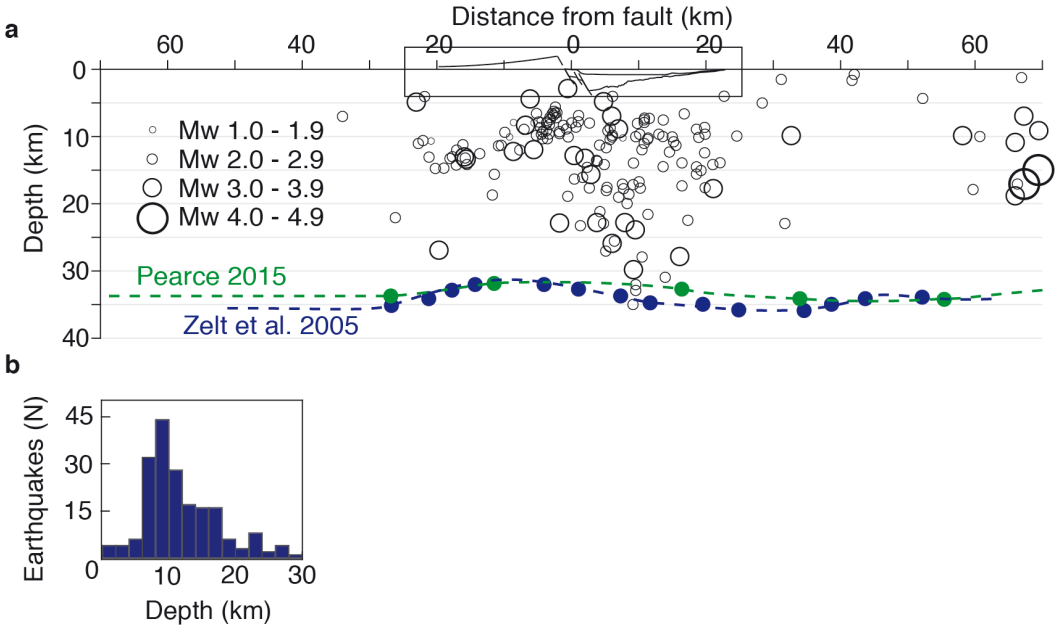


**Supplementary Figure 6: Crustal scale cross-section. (a)** Microseismicity from the University of Athens 1996-2008 earthquake catalogue measured within 2.5 km of profile A-A' in Fig. 1 and Moho depth estimates from Ps receiver functions[67] and tomographic inversion of PmP reflection times[68] **(b)** Histogram of (micro-)earthquake depths.

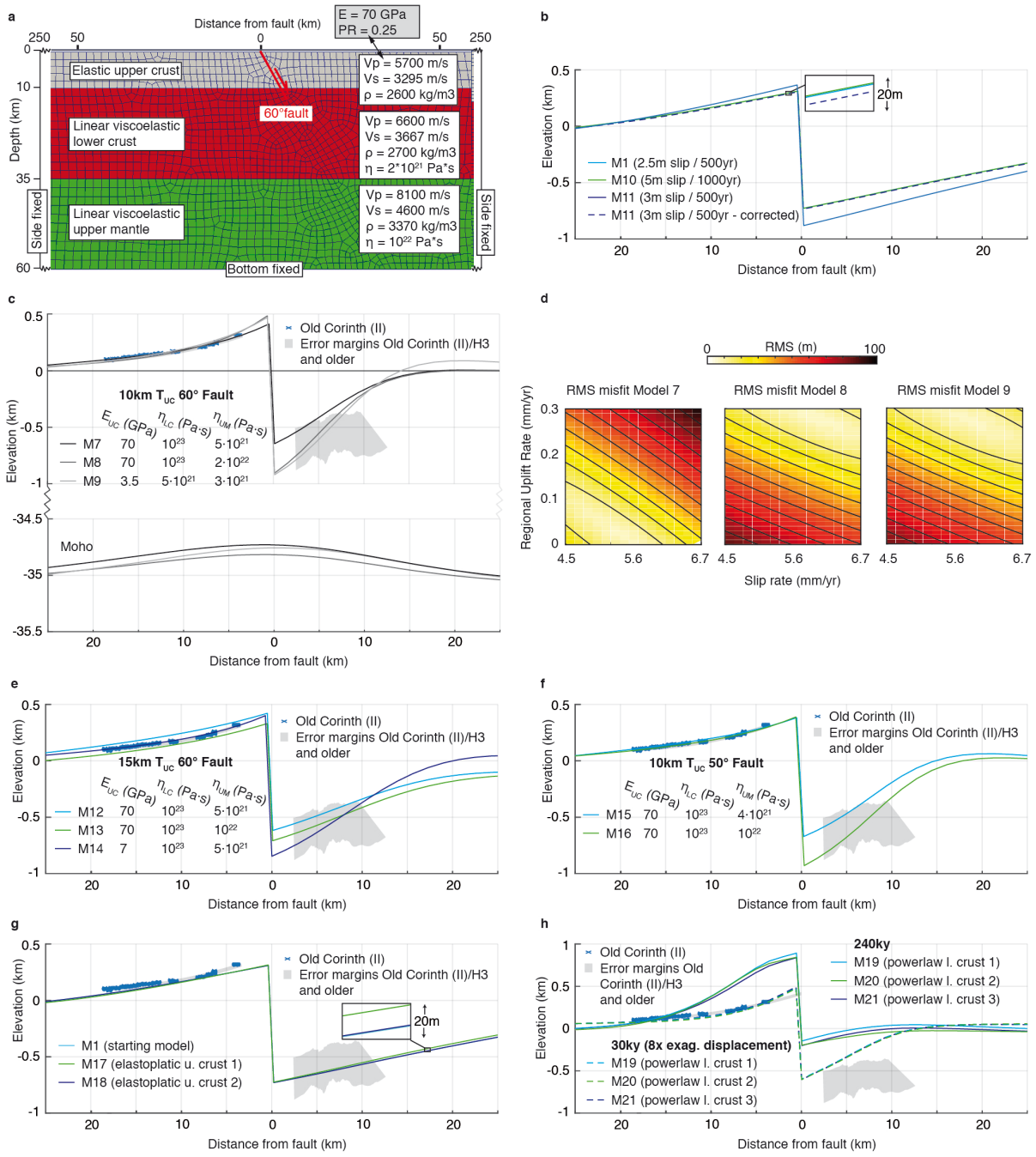


**Supplementary Figure 7: Additional fault modelling results. (a)** Subset of finite element grid showing Model 1 set-up. E = Young's Modulus, PR = Poisson's Ratio, Vp = P-wave velocity, Vs = S-wave velocity, ρ = density, η = viscosity **(b)** Tests on the influence of different earthquake recurrence time (M10) and slip rate (M11), the latter both uncorrected and with total displacement corrected by a factor 0.83 **(c)** Models 7-9 from Fig. 5b for comparison with **f-h (d)**

Root-mean-squared misfits of models 7-9 under the assumption of different fault slip rates and regional uplift rates. **(e)** Models with a 15km thick upper crust and 60° fault, for which good fits with the terrace data require the upper crustal Young's Modulus to be relatively low and the lower crustal viscosity to be relatively high in comparison to the models in **c (f)** Models with a 10 km thick upper crust and 50° fault, for which good fits with the terrace data require slightly lower upper mantle viscosities in comparison to the models in **c (g)** Models with an elastoplastic upper crust compared to Model 1 **(h)** Models with an elastoplastic upper crust and non-linear (powerlaw) viscoelastic lower crust compared to Model 1. Although on a ~30 ka timescale they produce a realistic surface deformation pattern, on the long term they become unstable and produce an unrealistically low U:S ratio.

**Supplementary Table 1: Input parameters for numerical fault models.** Resulting surface deformation pattern and moho geometry produced by these models after 240 ka are shown in Fig. 5 and Supplementary Fig. 7.

**Elastic upper crust – linear viscoelastic lower crust – linear viscoelastic upper mantle**

| Model Nr. | Young's Modulus U.Crust (GPa) | Upper Crustal Thickness (km) | Fault dip angle (°) | L. Crustal Viscosity (Pa·s) | U. Mantle Viscosity (Pa·s) |
|---|---|---|---|---|---|
| 1 | 70 | 10 | 60 | $2 \cdot 10^{21}$ | $10^{22}$ |
| 2 | 7 | 10 | 60 | $2 \cdot 10^{21}$ | $10^{22}$ |
| 3 | 70 | 15 | 60 | $2 \cdot 10^{21}$ | $10^{22}$ |
| 4 | 70 | 10 | 40 | $2 \cdot 10^{21}$ | $10^{22}$ |
| 5 | 70 | 10 | 60 | $10^{22}$ | $10^{22}$ |
| 6 | 70 | 10 | 60 | $2 \cdot 10^{21}$ | $10^{23}$ |
| 7 | 70 | 10 | 60 | $10^{23}$ | $5 \cdot 10^{21}$ |
| 8 | 70 | 10 | 60 | $10^{23}$ | $2 \cdot 10^{22}$ |
| 9 | 3.5 | 10 | 60 | $5 \cdot 10^{21}$ | $3 \cdot 10^{21}$ |
| 10* | 70 | 10 | 60 | $2 \cdot 10^{21}$ | $10^{22}$ |
| 11** | 70 | 10 | 60 | $2 \cdot 10^{21}$ | $10^{22}$ |
| 12 | 70 | 15 | 60 | $10^{23}$ | $5 \cdot 10^{21}$ |
| 13 | 70 | 15 | 60 | $10^{23}$ | $10^{22}$ |
| 14 | 7 | 15 | 60 | $10^{23}$ | $5 \cdot 10^{21}$ |
| 15 | 70 | 10 | 50 | $10^{23}$ | $4 \cdot 10^{21}$ |
| 16 | 70 | 10 | 50 | $10^{23}$ | $8 \cdot 10^{21}$ |

* Same parameters as model 1, but with 5m slip earthquakes every 1000 years instead of 2.5m slip earthquakes every 500 years

** Same parameters as model 1, but with 3m slip earthquakes every 500 years instead of 2.5m slip earthquakes every 500 years

**Elastoplastic upper crust – linear viscoelastic lower crust – linear viscoelastic upper mantle**

| Model Nr. | Cohesion (MPa) | Internal friction angle (°) | Dilatation angle (°) |
|---|---|---|---|
| 17* | 10 | 20 | 20 |
| 18* | 50 | 30 | 30 |

* All other parameters same as model 1

**Elastoplastic upper crust – non-linear (powerlaw) viscoelastic lower crust – linear viscoelastic upper mantle**

| Model Nr. | Temp. lower crust (°C) | Powerlaw stress exponent | Act. energy Q ($kJ \cdot mol^{-1}$) | Pre-exponential term A ($MPa^{-n} \cdot s^{-1}$) | U. Mantle Viscosity (Pa·s) |
|---|---|---|---|---|---|
| 19* | 300-720 | 4.0 | 223 | $1.1 \cdot 10^{-4}$ | $10^{22}$ |
| 20* | 300-650 | 4.0 | 223 | $1.1 \cdot 10^{-4}$ | $10^{22}$ |
| 21* | 300-720 | 4.0 | 223 | $1.1 \cdot 10^{-4}$ | $10^{23}$ |

* All other parameters same as model 18